Journal of Materials Chemistry B

Accepted Manuscript

ROYAL SOCIETY OF CHEMISTRY

www.rsc.org/materialsB

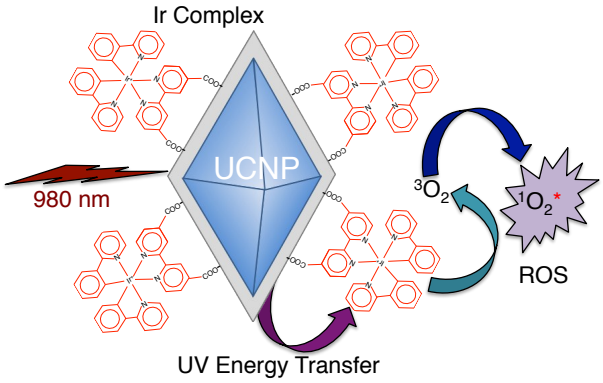

Journal Name

ARTICLE

Near-Infrared Triggered Generation of Reactive Oxygen Species from Upconverting Nanoparticles Decorated with an Organoiridium Complex

Received 00th January 20xx,
Accepted 00th January 20xx

DOI: 10.1039/x0xx00000x

www.rsc.org/

Joe Gerald Jesu Raj[a], Marta Quintanilla[a] and Fiorenzo Vetrone*[a, b]

Recently, research efforts have focused on developing near-infrared perturbable nanoparticles to sensitize photostimulable molecules for the production of reactive oxygen species. Research in this direction is looking to broaden the use of photodynamic therapy, an indispensable clinical tool for cancer therapeutics, which relies on the photoexcitation of a suitable photosensitizer, to convert light to reactive oxygen species that are toxic to cells. To date most commercially available photosensitizers are excited with high energy light (UV or visible) presenting disadvantages that limit the clinical use of this technique to cancers that are on or near the surface of the skin. Here, we develop a hybrid platform capable of near-infrared triggered generation of reactive oxygen species. This hybrid nanostructure is based on $LiYF_4$: Tm^{3+}, Yb^{3+} nanoparticles, which are capable of producing strong UV emissions, following excitation at 980 nm, through a multiphoton process known as upconversion. When appropriately surface functionalized with an organoiridium complex, excitation at 980 nm produces a strong UV emission, which is absorbed by the organoiridium molecules on the surface, in turn generating reactive oxygen species. Moreover, the effect of the organoiridium concentration on the surface of the upconverting nanoparticles as well as the nature of the sensitization process is discussed.

Introduction

Over the course of the last few years, transition metal-based complexes have garnered a great deal of attention for a variety of applications.[1,2] In particular, cyclometalated iridium (Ir) complexes are of significant interest due to their tunable properties, which can be altered by changing the ligands and their substituents around the metal center.[3] Their luminescence properties have been long studied since these luminescent complexes are well-known for their characteristic large Stokes shift, long lifetimes, tunable absorption and emission wavelengths, as well as high quantum yields, which are attributed to their *metal-ligand charge transfer* (MLCT) transitions.[4] These remarkable photophysical properties make Ir complexes amenable for a wide range of optoelectronic applications including biomedical imaging with particular focus on cancer. [5-7]

The influence of Ir complexes in the field of cancer research has not been limited to bioimaging applications. These complexes are being studied for use in cancer therapeutics particularly chemotherapeutics[8] and photodynamic therapy (PDT)[9]. In the latter light-based application, malignant cells are destroyed by cytotoxic reactive oxygen species (ROS). PDT uses a photoperturbable molecule, called a photosensitizer, which is excited with light at a specific wavelength. This stimulates the photosensitizer to the excited state in turn promoting energy transfer to neighboring molecular oxygen (typically present in tissues), generating the ROS[10]. PDT has been gaining prominence in cancer treatment due to several reasons, among them; it is less invasive than more conventional cancer therapies including surgery as well as chemo- and radiotherapies[11] Furthermore, cancer cells can be targeted very precisely thus reducing the damage to the surrounding healthy cells thereby minimizing the harsh side effects currently associated with cancer therapy. [12,13]

One of the main drawbacks of using these transition metal complexes, as well as other clinically used photosensitizers, for PDT applications, is the requirement for excitation of the photosensitizer with high energy UV or visible light.[14,15] Poor tissue penetration of high energy light hampers their use in living systems where cancers are buried deep within the body. The recent introduction of optical fiber based systems as a delivery tool for the excitation light has relieved some of these issues but the major use of this type of therapy is still focused on surface based cancers where the photosensitizer is applied topically.[16-19] A considerable body of work has focused on overcoming this drawback of tissue penetration by exploiting the use of near-infrared (NIR) excitation

[a] *Institut National de la Recherche Scientifique (INRS) - Énergie, Matériaux et Télécommunications (EMT), Université du Québec, Varennes, J3X 1S2 Québec, Canada*

[b] *Centre for Self-Assembled Chemical Structures, McGill University, Montreal, QC H3A 2K6, Canada*

† Footnotes relating to the title and/or authors should appear here.
Electronic Supplementary Information (ESI) available: [details of any supplementary information available should be included here]. See DOI: 10.1039/x0xx00000x

sources particularly in the region of about 700-1000 nm (the first biological window).[20] In this region, tissue penetration is typically large (*e.g.* cm penetration depths have been reported)[21] and both the autofluorescence and phototoxicity effects are negligible. For example, two-photon induced PDT has been reported where two NIR photons from an ultrafast laser (in the femtosecond range) could be simultaneously absorbed to excite the photosensitizer.[22,23] While this technique presents a number of advantages including the minimization of any out of focus photodamage since the two-photon absorption (TPA) occurs at the focal point[24], complex and expensive lasers are required thereby potentially delaying their adoption for clinical use.

An alternative for NIR excitation of a PDT photosensitizer involves the use of lanthanide-doped upconverting nanoparticles (UCNPs) as energy donors.[15,25] These nanoparticles have the inherent ability to convert low energy NIR excitation light (typically 800 or 980 nm) to higher energies covering the UV, visible and NIR portions of the spectrum *via* a multiphoton process referred to as upconversion.[26,27] Contrary to conventional TPA, upconversion occurs *via* the sequential absorption of NIR photons since the excitation process occurs through real excited states with long lifetimes in the μs to ms range. This has several advantages compared to TPA; first, ultrafast lasers are not required thus the multiphoton excitation can be carried out using an inexpensive, continuous wave diode laser. Second, the NIR triggered generation of ROS is more efficient since the upconversion process is typically more efficient than TPA.[28]

Various strategies have been presented for PDT using UCNPs. This involves a number of different host UCNPs such as $NaYF_4$[29], $NaGdF_4$[30], $LiYF_4$[31] and various sensitizers including zinc phthalocyanine[32], rose bengal[33], methylene blue[34], as well as many others.[35,36] The techniques for coupling the photosensitizers to the UCNPs in order to achieve NIR triggered generation of ROS were manifold and included encapsulation of both the UCNP (energy donors) and photosensitizer (acceptors) in silica[37], covalent conjugation through chemical bonding[38] and non-covalently physical adsorption.[39] In all cases, the NIR excitation photons were converted to higher energies *via* upconversion and this upconverted energy was subsequently transferred to the photosensitizer, either radiatively or non-radiatively, to induce the generation of the ROS. It is evident that when NIR perturbable UCNPs are coupled with UV or visible light triggered photosensitizers, the potential usefulness of this technique increases and opens up the possibility for the *in situ* generation of ROS, directly at the site of interest since the NIR excitation light can penetrate the skin. While a number of reports have been published on NIR-triggered generation of ROS, in particular for cancer PDT applications, the interest in upconversion based PDT is growing. There exists a great deal of interest in developing new UCNP/photosensitizer combinations as well as to investigate the mechanisms of photosensitization. The vast majority of work has focused on the $NaY(Gd)F_4$ system, in particular those nanoparticles co-doped with Er^{3+}/Yb^{3+} ions where their visible (green or red) upconverted emission was exploited to excited the photosensitizer. In our present work, we use the $LiYF_4$ host, which considerably underexplored and when doped with Tm^{3+}/Yb^{3+} ions has proven its ability to convert the NIR light to very intense UV light, which here is used to trigger the generation of ROS. In our present work, we have synthesized $LiYF_4:Tm^{3+},Yb^{3+}@SiO_2$ UCNPs decorated with a hydrophilic organoiridium complex to study the generation of ROS following excitation with 980 nm NIR radiation (Scheme 1), which to our knowledge is the first report on the use of an organoiridium complex for NIR triggered ROS generation. Moreover, the hydrophilic organoiridium complex possesses two carboxyl functional groups (-COOH), which are readily available for further bioconjugation of diverse biomolecules. Thus, the $LiYF_4:Tm^{3+}$, $Yb^{3+}@SiO_2@Ir$ nanostructure can serve as a scaffold on which to build even more functionality.

Experimental

Materials and Chemicals

Aqueous ammonia solution ($NH_3 \cdot H_2O$, 28%), tetraethylorthosilicate (TEOS > 98%), anhydrous ethanol, 2-phenylpyridine, $IrCl_3 \cdot 3H_2O$, 2-ethoxyethanol, 2,2'-bipyridine-4,4'-dicarboxylic acid, sodium acetate, ammonium hexafluorophosphate, 1,3-Diphenylisobenzofuran (DPBF) (97%), silica gel (Pore size 60 Å, 200-425 mesh particle size) were purchased from Sigma Aldrich. Y_2O_3 (99.99%), Yb_2O_3 (99.9%), Tm_2O_3 (99.99%), trifluoracetic acid (CF_3COOH), lithium trifluoroacetate (CF_3COOLi), oleic acid, 1-octadecene (OD), were obtained from Alfa Aesar. IGEPAL CO-520, methanol, hexane, cyclohexane, dichloromethane, acetone, ammonia solution (25%, w/w), hydrochloric acid were purchased from Fluka (USA). Highly pure water (Millipore) of resistivity greater than 18.0 MΩ cm was used in all experiments. All chemicals were used as received unless specified.

Instrumentation

The Fourier-transform infrared (FTIR) spectra were recorded on a Thermoscientific Nicolet Spectrometer using FTIR grade KBr as the background. Transmission Electron Microscopy (TEM) images were obtained with a Philips Tecnai 12 (120 kV) microscope. To observe the morphology and size distribution of the UCNPs, 10 mg of the UCNP sample was dispersed in 10 g of hexane and sonicated for 1 h. A drop of the resulting solution was evaporated on a formvar/carbon film supported on a 300 mesh copper grid (3 mm in diameter). X-ray photoelectron spectroscopy (XPS) analyses were performed on a VG Escalab 220i XL instrument equipped with 6 channeltrons using a non-monochromated Mg K X-ray source (1253.6 eV). To identify the phase of the UCNPs, X-ray diffraction (XRD) patterns were recorded using a Bruker D8 Advance Powder Diffractometer with Cu Kα radiation at $\lambda = 0.154$ nm operating at 45 kV and 40 mA. The UV-Vis absorption measurements were carried out using a Thermoscientific 2000 spectrophotometer. Dynamic light scattering (Malvern, Zetasizer Nano S90) was used to determine the hydrodynamic radius of the $LiYF_4:Tm^{3+},Yb^{3+}@SiO_2@Ir$ nanostructures. Accurate mass measurements were performed on

an LC/MSD-TOF mass spectrometer system from Agilent Technologies in positive electrospray mode. Protonated molecular ions, (M+H)+ and molecular ions, M+ were used for empirical formula confirmation.

The upconversion emission spectra were obtained using a Thorlabs fiber-coupled 980 nm laser diode (maximum power of 330 mW) as the excitation source. For the oleate-capped hydrophobic UCNPs, the samples (1 wt% in hexane) were placed in 10 mm path-length quartz cuvettes (Hellma, QS). The upconverted emission light was collected by a lens in a 90^{o} configuration, and then transferred to a spectrophotometer (Avaspec-2048L-USB2) using an optical fiber. Throughout the course of the experiments, the cuvette was placed in a fixed sample holder that guarantees a comparable laser focalization for every sample, and thus, the possibility to compare intensities between different samples. To confirm this, every spectrum was recorded multiple times.

Synthesis of Precursor Complex $[(ppy)_2Ir(\mu\text{-}Cl)]_2$

The organoiridium (Ir) complex was synthesized according to the literature procedure with a slight modification.[40,41] Briefly, a mixture of 2-phenylpyridine (0.34 g, 2.2 mmol), $IrCl_3 \cdot 3H_2O$ (0.34 g, 1 mmol) in a mixed solvent of 2-ethoxyethanol (15 mL) and water (5 mL) was stirred under N_2 at 120 ^{o}C for 20 h. The precipitate was then cooled to room temperature and collected by filtration and washed with water, ethanol, acetone, respectively, and subsequently dried in vacuum to give the $[(ppy)_2Ir(\mu\text{-}Cl)]_2$ dimer complex. Mass spectra of the precursor showed a molecular ion peak at m/z: 1072 thus confirming its successful synthesis (Fig. S1, top).

Synthesis of $[(ppy)_2Ir(dcbpy)]^+ PF_6^-$

$[(ppy)_2Ir(\mu\text{-}Cl)]_2$ (0.21 g, 0.2 mmol) was prepared as a solution in dichloromethane (15 mL) and added to a suspension of 2,2'-bipyridine-4,4'-dicarboxylic acid (0.098 g, 0.4 mmol) in methanol (20 mL). The reaction mixture was then heated to reflux with stirring for 4 h. To this solution, excess sodium acetate in methanol (5 mL) was added, and the mixture was stirred for 45 min. The solvent was then removed under reduced pressure. Then, hydrochloric acid (1 M, 10 mL) was added, and the suspension was stirred for 20 min. The product was then filtered, washed with water (2 × 25 mL), vacuum dried, and the solid was then dissolved in methanol. A saturated solution of ammonium hexafluorophosphate in methanol (5 mL) was then added, and the mixture was stirred for a further 45 min. The solvent was removed under reduced pressure, and the residue was extracted into dichloromethane and filtered. The solvent was removed under reduced pressure to yield $[(ppy)_2Ir(dcbpy)]^+ PF_6^-$ as a dark-red powder. The crude product was flash chromatographed on silica gel using CH_2Cl_2 as an eluent to afford the desired Ir complex. (0.16 g, 69%). Mass spectra of the final complex showed a molecular ion peak at m/z: 745 thus confirming the successful synthesis of the final organoiridium complex. The high intensity of the signals also confirmed that they are the predominant products (Fig. S1, bottom).

Synthesis of Oleate-Capped $LiYF_4$: Tm^{3+}, Yb^{3+} UCNPs

The thulium (Tm^{3+}) and ytterbium (Yb^{3+}) co-doped $LiYF_4$ UCNPs (0.5 mol% Tm^{3+} and 25 mol% Yb^{3+}) were synthesized via the thermal decomposition method as described previously.[42,43] Briefly, the lanthanide trifluoroacetate precursors were prepared by reacting Y_2O_3 (1 mmol), Yb_2O_3 (0.27 mmol), Tm_2O_3 (0.005 mmol) in 50/50 v/v CF_3COOH/H_2O at 80 °C for 6 h. Then the resultant clear solution was evaporated to dryness at 60 °C overnight. The obtained lanthanide trifluoroacetates precursors were mixed with CF_3COOLi (2.5 mmol), oleic acid (20 mL) and 1-octadecene (20 mL). The resulting mixture was degassed to 110 °C with constant stirring under vacuum for 30 min. Subsequently, the temperature of the mixture was increased to 330 °C at a rate of 5 °C/min under Ar flow. At this final temperature, the mixture remained for 1 h, after which it was allowed to cool to 70 °C prior to precipitation with ethanol. The $LiYF_4$:Tm^{3+}, Yb^{3+} UCNPs were then separated via centrifugation and further purified by redispersing in hexane followed by precipitation with ethanol three times.

Synthesis of $LiYF_4$: Tm^{3+}, Yb^{3+}@SiO_2 UCNPs

The silica (SiO_2) shell around the $LiYF_4$:Tm^{3+}, Yb^{3+} UCNPs was grown by mixing 20 mg of the UCNPs dispersed in cyclohexane with 0.1 mL Igepal and 6 mL cyclohexane. After 10 min stirring, 0.4 mL Igepal and 0.08 mL NH_4OH were added to the above flask and sonicated for 20 min. Once the mixture became transparent, 0.04 mL TEOS was added and left to stir for 48 h. The silica-coated $LiYF_4$:Tm^{3+}, Yb^{3+} UCNPs were separated by adding acetone, and subsequently washed with ethanol/water (1:1) twice.

Synthesis of $LiYF_4$: Tm^{3+}, Yb^{3+}@SiO_2@$[(ppy)_2Ir(dcbpy)]^+ PF_6^-$

5 mg of the Ir complex was dissolved in 10 mL of ethanol containing 10 mg of $LiYF_4$: Tm^{3+}, Yb^{3+}@SiO_2. After stirring for 12 h, the $LiYF_4$: Tm^{3+}, Yb^{3+}@SiO_2 UCNPs decorated with the Ir complex (henceforth UCNPs@SiO_2@Ir) were separated by centrifugation and washed with ethanol. Loading efficiency of the Ir complex on the $LiYF_4$: Tm^{3+}, Yb^{3+}@SiO_2 UCNPs was measured by UV–Vis absorption spectroscopy and determined to be ~60% (Fig. S2).

Detection of Reactive Oxygen Species (ROS)

The generation of ROS was measured with a 1,3-diphenylisobenzofuran (DPBF) probe. In a typical process, 10 mg of the $LiYF_4$:Tm^{3+}, Yb^{3+}@SiO_2@Ir nanostructures were well dispersed in 2 mL of DPBF solution (5 x 10^{-5} M in 1:1 water:ethanol) with ultrasonic processing in the dark. The mixture was irradiated with the 980 nm NIR laser (with a power density of 185 W/cm^2) for various time periods, always applying magnetic stirring to guarantee the homogeneous distribution of the different components in the solution for the duration of the experiment. The generation of ROS was confirmed by the characteristic absorption decrease of the DPBF using a UV-Vis absorption spectrum.

Results and discussion

The main objective of the UCNPs@SiO_2@Ir nanostructured system designed in this work was to sensitize the Ir complex *via* the upconverted UV radiation due to its strong absorption in the UV region (*vide infra*). Hence, UCNPs with intense upconverted UV emissions were required. Amongst a number of strong UV-emitting UCNPs,[44-46] $LiYF_4$:Tm^{3+}, Yb^{3+} was chosen since it has intense upconverted UV emissions that have been shown to be capable of sensitizing other light activated processes.[47,48] Thus, at the onset, monodispersed $LiYF_4$: Tm^{3+}, Yb^{3+} UCNPs were synthesized by the thermal decomposition method where oleic acid was used as the surface capping ligand and 1-octadecene as the high temperature boiling solvent.[43]

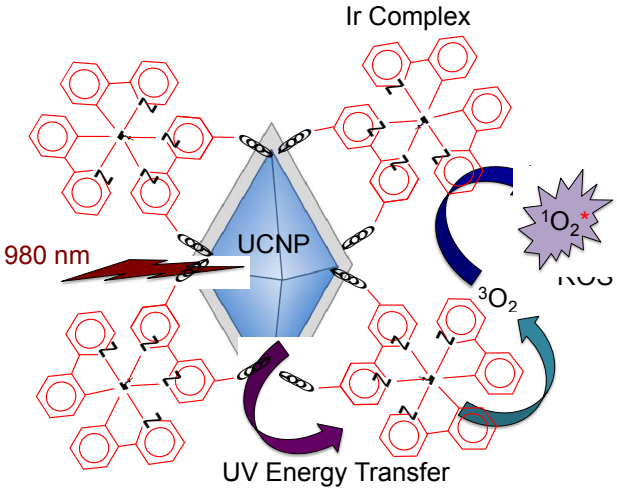

Scheme 1. 980 nm excitation of the $LiYF_4$:Tm^{3+}, Yb^{3+}@SiO_2@Ir nanostructure for the NIR triggered generation of reactive oxygen species.

As seen in the TEM image in Fig. 1A, the $LiYF_4$:Tm^{3+}, Yb^{3+} UCNPs crystallized with a square bipyramidal morphology possessing a mean particle size of approximately 65 nm (in width) and 110 nm (in length) with an aspect ratio of 1.73 (Fig. 1C). The synthesized UCNPs were highly dispersible in the major organic non-polar solvents such as toluene and hexane. However, the aim of this work was to study the NIR triggered release of ROS for future applications in *in vitro* and *in vivo* biological experiments, therefore, their dispersibility in aqueous media was of critical importance. Hence, the synthesized UCNPs with hydrophobic oleate surface capping ligands were rendered water dispersible by growing a thin layer of SiO_2 on their surface. The TEM image (Fig. 1B) demonstrates the homogeneity and thickness of the SiO_2 shell around the UCNPs, which was determined to be circa 13 nm. Furthermore, the DLS measurements revealed an average particle diameter of 135 nm (Fig. S3). It is important to note that this slight discrepancy compared to the TEM data is due to the fact that DLS provides information on the hydrodynamic diameter of the nanostructures when dispersed in a solvent (in this case PBS buffer) while TEM images provide information about the particle size in the dry state. Encapsulation of the UCNPs with an SiO_2 layer endowed a negative charge on its surface. Since the synthesized cyclometalated organoiridium complex is cationic because of the positive charge on the central iridium atom, this octahedral iridium complex could be directly adsorbed through strong electrostatic force of attraction thus yielding the $LiYF_4$@SiO_2@Ir nanostructure.

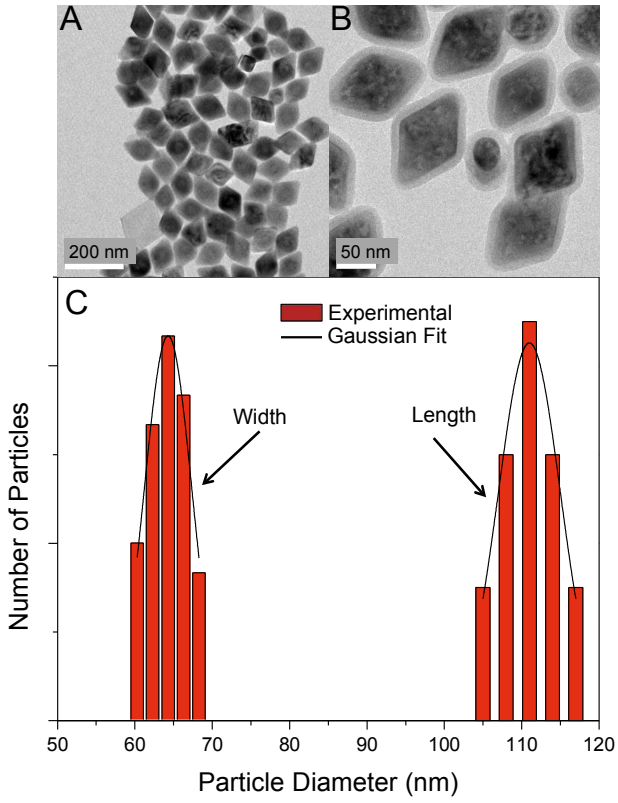

Fig. 1 (A) Characteristic TEM image of the oleate-capped $LiYF_4$:Tm^{3+}, Yb^{3+} and (B) $LiYF_4$: Tm^{3+}, Yb^{3+}@SiO_2 UCNPs. (C) Particle size distribution of the oleate-capped UCNPs showing both the lengths and the widths. The aspect ratio was calculated to be approximately 1.73.

The crystalline nature of the UCNPs was confirmed by X-ray powder diffraction (XRD) analysis (Fig. S4). All the peaks in XRD were well indexed in accordance with the standard pattern of tetragonal phase $LiYF_4$ (JCPDS No. 01–077–0816), confirming the absence of any impurity in the UCNPs synthesized here. The FTIR analysis (Fig. S5A) of the parent oleate-capped UCNPs revealed the presence of carboxylic acid functional groups (black line). The peaks at 1460 and 1562 cm^{-1} were due to carboxylate symmetrical and asymmetrical stretching vibrations, respectively. In addition, the strong absorption bands at 2852 and 2938 cm^{-1} were attributed to the symmetrical and asymmetrical C–H stretching vibrations of the aliphatic chain of the oleate capping ligand. Furthermore, the band at approximately 3450 cm^{-1} was due to the O-H stretching vibration. Following modification of the $LiYF_4$:Tm^{3+}, Yb^{3+} UCNPs with the silica shell (blue line), the intensities of C-H symmetrical and asymmetrical vibrations were reduced. However, a broad peak appears at 1126 cm^{-1}, which was attributed to the Si-O-Si stretching vibration and the peak at 982 cm^{-1} was the result of the Si-O-Si bending vibration. Furthermore, the successful conjugation of the

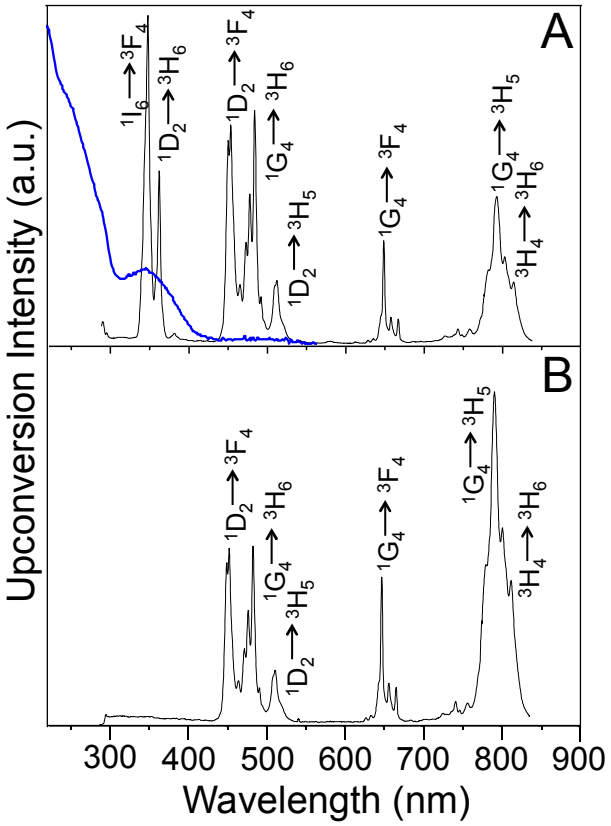

Fig. 2 (A) Absorption spectrum of the synthesized organoiridium complex (blue line) and upconversion luminescence spectrum of the $LiYF_4:Tm^{3+}$, $Yb^{3+}@SiO_2$ UCNPs (black line) and (B) upconversion luminescence spectrum of the UCNPs following functionalization with the cyclometalated Ir complex. λ_{exc} = 980 nm.

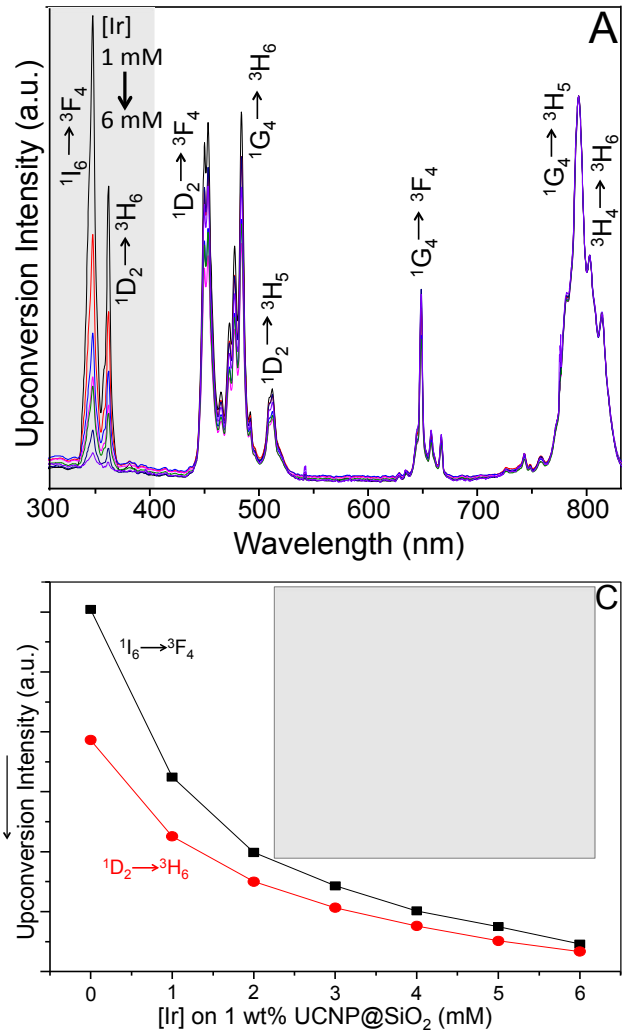

Fig. 3 (A) Total upconversion emission spectra of the of $LiYF_4:Tm^{3+}$, $Yb^{3+}@SiO_2$ UCNPs obtained following functionalization with different concentrations of the Ir complex. The spectra were normalized to the NIR emission band. The inset (B) shows the expanded region between 300-400 nm where quenching is observed. (C) Plot demonstrating the decrease in the UV emission intensity upon increased concentration of Ir complex for the $LiYF_4:Tm^{3+}$, $Yb^{3+}@SiO_2$@Ir nanostructures. λ_{exc} = 980 nm.

cationic Ir complex on the negatively charged silica surface (UCNPs@SiO_2@Ir) was confirmed by the appearance of all major functional groups in the FTIR spectrum. The peaks at 2984, 1728, and 852 cm^{-1} were due to the O-H, carbonyl stretching frequencies of the carboxylic acid functional groups and PF vibrations, respectively. The final UCNPs@SiO_2@Ir nanostructures were further confirmed by XPS measurements where peaks ascribed to all the major constituents of this material were observed (Fig. S5B). This includes peaks from the metal ions in the host nanocrystal (Li and Y), the lanthanide dopants (Tm and Yb) as well as the Ir complex functionalized to the UCNPs@SiO_2 surface.

Upon excitation of the UCNPs@SiO_2 with NIR light (at 980 nm), multiple, sharp upconverted emission peaks in the regions spanning the UV to NIR were observed, which were the result of the sequential absorption of multiple 980 nm NIR photons. (Fig. 2A, black line). The upconverted UV emissions at 345 and 360 nm were assigned to the $^1I_6 \rightarrow {}^3F_4$ and $^1D_2 \rightarrow {}^3H_6$ transitions, respectively while the blue upconversion emissions observed at 450 and 480 nm were assigned to the $^1D_2 \rightarrow {}^3F_4$ and $^1G_4 \rightarrow {}^3H_6$ transitions, respectively. At lower energies, the red emission centered at 650 nm was ascribed to the $^1G_4 \rightarrow {}^3F_4$ transition while the NIR emission at 800 nm resulted from the $^3H_4 \rightarrow {}^3H_6$, $^1G_4 \rightarrow {}^3H_5$ transitions. The mechanism of Tm^{3+}/Yb^{3+} upconversion is demonstrated in Fig. S6.

For comparative purposes, the UV-Vis absorption spectrum of the cyclometalated Ir complex, $[(ppy)_2Ir(dcbpy)]^+PF_6^-$, presented in Fig. 2A (blue line), showed the two characteristic absorption peaks centered at wavelengths 290 nm and 380 nm corresponding to ligand centered (LC) and MLCT transitions, respectively.[41] Thus, the absorption spectrum of the Ir complex shows a good spectral overlap with the upconverted emission spectrum of the $LiYF_4:Tm^{3+},Yb^{3+}@SiO_2$ UCNPs (Fig. 2A, black line). This overlap brings forth the possibility of effective energy transfer between the UCNPs (in the $^1I_6$ and $^1D_2$ excited states of the Tm^{3+} ions) and the Ir complex on their surface. The interaction between the UCNPs@SiO_2 and the Ir complex would result in the quenching of the Tm^{3+} UV emissions, as the energy is absorbed by the organoiridium

molecules. This is manifested in the upconversion spectra of the $LiYF_4$:Tm^{3+},Yb^{3+}@SiO_2 UCNPs after functionalization with the Ir complex, where the previously mentioned transitions in the UV range completely disappeared (Fig. 2B).

The key question is whether the energy transfer between the UCNPs@SiO_2 (energy donor) and the Ir complex (acceptor) on the surface is radiative or non-radiative. This question can be answered by looking at the upconverted blue emission in the spectrum of the $LiYF_4$:Tm^{3+},Yb^{3+}@SiO_2@Ir nanostructures (Fig. 2B). It is clear that the UV emissions emanating from the $^1I_6 \rightarrow {}^3F_4$ and $^1D_2 \rightarrow {}^3H_6$ transitions are completely quenched. However, in the blue range, the emissions are still present. These emissions correspond to three different transitions, with two of them originating from the excited $^1D_2$ state ($^1D_2 \rightarrow {}^3F_4$ and $^1D_2 \rightarrow {}^3H_5$), the same energy state that is at the origin of the UV emission. Thus, the fact that the UV emission from the $^1D_2$ state is totally quenched by the Ir complex, while the blue emissions remain almost unaffected, indicates that the energy transfer occurs, to a large extent, after the emission of photons in the $LiYF_4$:Tm^{3+}, Yb^{3+}@SiO_2 UCNPs, i.e., the energy transfer process appears to be predominantly radiative. The $^1G_4$ excited state lies outside absorption window of the Ir complex (~475 nm) and if non-radiative energy transfer were present, the blue $^1D_2$ emissions ($^1D_2 \rightarrow {}^3F_4$ and $^1D_2 \rightarrow {}^3H_5$) would be quenched while the blue $^1G_4$ emission ($^1G_4 \rightarrow {}^3H_5$) should remain unchanged. This would manifest as a change in the relative intensities of the blue bands, which is not case. Furthermore, the SiO_2 layer covering $LiYF_4$ UCNPs imposes a spatial separation with the organoiridium complex (of approximately 13 nm, according to Fig. 1B) further minimizing the chances of non-radiative energy transfer.

To further probe the nature of the UV quenching, different concentrations of the cationic Ir complex were functionalized on the surface of the $LiYF_4$:Tm^{3+}, Yb^{3+}@SiO_2 UCNPs. This resulted in different quenching of the upconverted UV emissions emanating from the $LiYF_4$:Tm^{3+}, Yb^{3+}@SiO_2@Ir nanostructures (Fig. 3A). This behaviour is more clearly demonstrated in the inset Fig. 3A, where to facilitate the comparison, the emission intensities of the different samples were normalized to the NIR emission band of Tm^{3+} (800 nm), as the Ir complex absorption is non-existent at this wavelength. Moreover, the Fig. 3C demonstrates that the decrease in the UV emission intensities for both the $^1I_6 \rightarrow {}^3F_4$ and $^1D_2 \rightarrow {}^3H_6$ transitions were not linear.

As previously mentioned, the photosensitization of the Ir complex, *via* the upconverted radiation, can interact with the surrounding oxygen molecules to produce the ROS. To study this, the $LiYF_4$:Tm^{3+}, Yb^{3+}@SiO_2@Ir nanostructures were dispersed in the solution containing the probe molecule, DPBF. With this method, the NIR triggered generation of ROS by the $LiYF_4$: Tm^{3+}, Yb^{3+}@SiO_2@Ir nanostructures can be indirectly monitored by a decrease in the absorption spectra of the probe molecule DPBF, which shows a strong absorption at 420 nm (Fig. 4A). DPBF is highly reactive in the presence of $^1O_2$, decomposing it, and as a result, absorption at this wavelength decreases in the presence of $^1O_2$. The decrease in the absorption intensity is directly proportional to the amount of $^1O_2$ produced in the sample.[49]

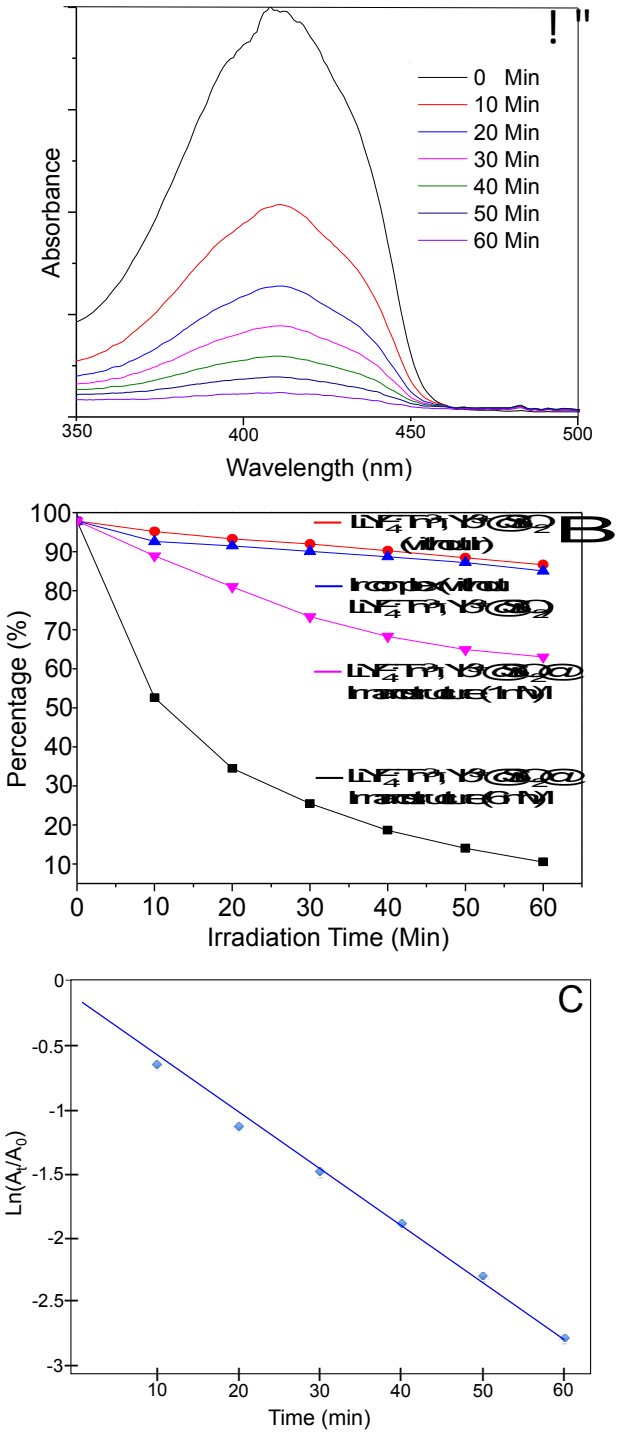

Fig. 4 (A) Decrease in the absorption of DPBF probe molecule in the presence of $LiYF_4$:Tm^{3+}, Yb^{3+}@SiO_2 UCNPs decorated with the Ir complex at various time intervals. (B) Comparison of the absorbance peak of DPBF at 420 nm after NIR irradiation at different times and for various samples, including $LiYF_4$: Tm^{3+}, Yb^{3+}@SiO_2 without Ir complex, $LiYF_4$: Tm^{3+}, Yb^{3+}@SiO_2 functionalized with two different concentrations of Ir complex (1 mM and 6 mM), and the Ir complex alone (i.e. without UCNPs). (C) Comparative plot of $Ln(A_t/A_0)$ as a function of time. A_0 is the initial absorbance, and A_t is the absorbance at irradiation times at different 980 nm NIR irradiation times.

To measure the ROS release, the UCNPs@SiO_2@Ir nanostructures were dispersed in an aqueous solution containing the probe molecule DPBF, which was irradiated using the 980 nm NIR laser (185 W/cm^2) at various time intervals. The absorption spectra were recorded after every ten minutes of irradiation (Fig. 4A). Plotting the maximum absorbance (at 420 nm) of DPBF against exposure time (Fig. 4B, black and magenta lines) clearly demonstrated that there was a steady decrease in the absorption of the probe molecule when the Ir complex was functionalized on the $LiYF_4$:Tm^{3+}, Yb^{3+}@SiO_2 UCNPs, thereby confirming the production of ROS. Furthermore, a higher concentration of Ir complex on the surface produces a faster decomposition of DPBF (black line), which is consistent with the proposed NIR triggered mechanism. To confirm that the generation of ROS is strictly due to the presence of the Ir complex and that it is activated through UCNPs, two control experiments were performed. First, we investigated the possibility of ROS generation with only the Ir complex (i.e. in the absence of the UCNPs@SiO_2) following excitation with 980 nm. Since the Ir complex has no absorption at this NIR wavelength, no ROS generation was expected (blue line in Fig. 4B). As demonstrated in Fig. 4B, this is in fact the case. Similarly, we investigated the possibility that only the $LiYF_4$:Tm^{3+}, Yb^{3+}@SiO_2 UCNPs (i.e. in the absence of the Ir complex) could generate ROS since UV light itself can induce photo-oxidation (red line in Fig. 4B). The observed effect in this case is, within the experimental error, the same as with the organoiridium complex alone, demonstrating that the production of ROS following NIR excitation requires both the UCNPs@SiO_2 and the Ir complex. Both control experiments show a small decrease with irradiation time that can be related to the effect of environmental light during several steps of the experiment. Fig. 4C shows the logarithmic ratio between the absorbance (A_t) of the probe DPBF molecule in the presence of the Ir decorated UCNPs@SiO_2 at various time intervals after 980 nm irradiation, and its original value (A_0) before irradiation. The plot gives an excellent linear fit with a negative slope of 0.04 corresponding to the photo-oxidation rate of the probe molecule. The negative slope confirms the fact that absorbance of the probe decreases along the y axis while irradiation time increases along the x axis with good linear regression value of 0.99264. Therefore, it is clear from the data in Fig. 4 that the presence of the cyclometalated Ir complex is a prerequisite for the efficient production of ROS when in close proximity to the NIR perturbable UCNPs@SiO_2.

Conclusions

In summary we have synthesized monodispersed $LiYF_4$:Tm^{3+}, Yb^{3+} UCNPs (65 nm in width and 110 nm in length) and coated them with a 13 nm shell of SiO_2 to render them hydrophilic. The UCNPs were subsequently functionalized with varying concentrations of an organoiridium complex on their surface. The photophysical properties of these $LiYF_4$:Tm^{3+}, Yb^{3+}@SiO_2@Ir nanostructures were investigated and it was demonstrated that upon surface functionalization with the Ir complex, a complete quenching of the upconverted UV emission from the Tm^{3+} ions was observed. Following absorption of the upconverted UV light, the Ir complex demonstrated a capacity to generate ROS, which was measured in the presence of a probe molecule (DPBF). Spectroscopic studies of the upconversion luminescence showed that the photosensitization of the Ir complex was radiative in nature. To confirm that the generation of ROS was in fact due to photosensitization of the Ir complex from the UCNPs, two control experiments were carried out. First, $LiYF_4$:Tm^{3+}, Yb^{3+}@SiO_2 UCNPs alone (without the Ir complex) were studied to observe if the upconverted UV light itself was capable of generating ROS. Second, the Ir complex alone was studied following excitation at 980 nm. In both cases, no ROS was observed indicating that both the UCNPs and Ir complex are required to generate ROS. This newly developed $LiYF_4$:Tm^{3+}, Yb^{3+}@SiO_2@Ir platform lays the foundation for the NIR triggered generation of ROS, which effectively eliminates the need for low penetrating, high energy external UV excitation, normally required for such photosensitizers.

Acknowledgements

FV is grateful to the Natural Sciences and Engineering Council (NSERC) of Canada and the Fonds de recherche du Québec - Nature et technologies (FRQNT) for funding his research.

References

1 K. Kalyanasundaram, M. Gratzel, *Coord. Chem. Rev*., 1998, **177**, 347-414.
2 E. Holder, B. M. W. Langeveld, U. S. Schubert, *Adv. Mater*., 2005, **17**, 1109-1121.
3 S. Lamansky, P. Djurovich, D. Murphy, F. A. Razzaq, H. E. Lee, C. Adachi, P. E. Burrows, S. R. Forrest, M. E. Thompson, *J. Am. Chem. Soc*., 2001, **123**, 4304-4312.
4 V. Balzani, A. Juris, M. Venturi, S. Campagna, S. Serroni, *Chem. Rev*., 1996, **96**, 759-834.
5 L. He, Y. Li, C. P. Tan, R. R. Ye, M. H. Chen, J. J. Cao, L. N. Ji, Z. W. Mao, *Chem. Sci*., 2015, **6**, 5409-5418.
6 Y. You, Y. Han, Y. M. Lee, S. Y. Park, W. Nam, S. J. Lippard, *J. Am. Chem. Soc.*, 2011, **133**, 11488-11491.
7 L. Murphy, A. Congreve, L. O. Palsson, J. A. G. Williams, *Chem. Commun.*, 2010, **46**, 8743-8745.
8 Z. Liu, L. Salassa, A. Habtemariam, A. M. Pizarro, G. J. Clarkson, P. J. Sadler, *Inorg. Chem*., 2011, **50**, 5777-5783.
9 R.-R. Ye, C.-P. Tan, L. He, M.-H. Chen, L.-N. Jia, Z.-W. Mao, *Chem. Commun.*, 2014, **50**, 10945-10948.
10 D. E. Dolmans, D. Fukumura, R. K. Jain, *Nat. Rev. Cancer*, 2003, **3**, 380-387.
11 B. C. Wilson, *Can. J. Gastroenterol.* 2002, **16**, 393-396.
12 R. Bonnett, *Chem. Soc. Rev.*, 1995, **24**, 19-33.
13 T. J. Dougherty, C. J. Gomer, B. W. Henderson, G. Jori, D. Kessel, M. Korbelik, J. Moan, Q. Peng, *J. Natl. Cancer Inst*., 1998, **90**, 12, 889-905.

14 A. P. Castano, P. Mroz, M. R. Hamblin, *Nat. Rev. Cancer*, 2006, **6**, 535-545.
15 N. M. Idris, M. K. Gnanasammandhan, J. Zhang, P. C. Ho, R. Mahendran, Y. Zhang. *Nat. Med*., 2012, **18**, 1580-1585.
16 Q. Peng, T. Warloe, K. Berg, J. Moan, M. Kongshaug, K. E. Giercksky, J. M. Nesland, *Cancer*, 1997, **79**, 2282-2308.
17 L. R. Braathen, R. M. Szeimies, N. B. Seguin, R. Bissonnette, P. Foley, D. Pariser, R. Roelandts, A. M. Wennberg, C. A. Morton, *J. Am. Acad. Dermato*., 2007, **56**, 125-143.
18 R. Allison, K. Moghissi, G. Downie, K. Dixon, *Photodiagn. Photodyn. Ther*. 2011, **8**, 231-239.
19 A. Juarranz, P. Jaén, F. Sanz-Rodríguez, J. Cuevas, S. González, *Clin. Transl. Oncol.*, 2008, **10**, 148-154.
20 P. Majumdar, X. Yuan, S. Li, B. Le Guennic, J. Ma, C. Zhang, D. Jacquemin, J. Zhao, *J. Mater. Chem. B*, 2014, **2**, 2838-2854.
21 R. Weissleder, *Nature Biotechnol*., 2001, **19**, 316-317.
22 R. M. Edkins, S. L. Bettington, A. E. Goeta, A. Beeby, *Dalton Trans*., 2011, **40**, 12765-12770.
23 J. D. Bhawalkar, N. D. Kumar, C. F. Zhao, P. N. Prasad, *J. Clin. Laser Med. Surg.,* 1997, **15**, 201-204.
24 L. M. Maestro, J. E. Ramírez-Hernández, N. Bogdan, J. A. Capobianco, F. Vetrone, J. G. Solé, D. Jaque, *Nanoscale*, 2012, **4**, 298-302.
25 D. K. Chatterjee, L. S. Fong, Y. Zhang, *Adv. Drug Deliv. Rev*., 2008, **60**, 1627-1637.
26 G. Chen, H. Qiu, P. N. Prasad, X. Chen, *Chem. Rev.*, 2014, **10**, 114, 5161-5214.
27 F. Auzel, *Chem. Rev*., 2004, **104**, 139-173.
28 L. M. Maestro, E. M. Rodriguez, F. Vetrone, R. Naccache, H. Loro Ramirez, D. Jaque, J. A. Capobianco and J. García Solé, *Opt. Express*, 2010, **18**, 23544-23553.
29 L. Zeng, Y. Pan, Y. Tian, X. Wang, W. Ren, S. Wang, G. Lu, A. Wu, *Biomaterials*, 2015, **57**, 93- 106.
30 X. Wang, K. Liu, G. Yang, L. Cheng, L. He, Y. Liu, Y. Li, L. Guo, Z. Liu, *Nanoscale*, 2014, **7**, 9198-9205.
31 M. Wang, Z. Chen, W. Zheng, H. Zhu, S. Lu, E. Ma, D. Tu, S. Zhou, M. Huang, X. Chen, *Nanoscale*, 2014, **6**, 8274-8282.
32 D. K. Chatterjee, Z. Yong, *Nanomedicine*, 2008, **3**, 73-82.
33 Q. Chen, C. Wang, L. Cheng, W. He, Z. Cheng, Z. Liu, *Biomaterials*, 2014, **35**, 2915-2923.
34 F. Chen, S. Zhang, W. Bu, Y. Chen, Q. Xiao, J. Liu, H. Xing, L. Zhou, W. Peng, J. Shi, *Chem. Eur. J*., 2012, **18**, 7082-7090.
35 C. Wang, H. Tao, L. Cheng, Z. Liu, *Biomaterials*, 2011, **32**, 6145-6154.
36 J. Shan, S. J. Budijono, G. Hu, N. Yao, Y. Kang, Y. Ju, R. K. Prud'homme, *Adv Funct Mater*., 2011, **21**, 2488-2495.
37 H. S. Qian, H. C. Guo, P. C. Ho, R. Mahendran, Y. Zhang, *Small*, 2009, **5**, 2285-2290.
38 K. Liu, X. Liu, Q. Zeng, Y. Zhang, L. Tu, T. Liu, X. Kong, Y. Wang, F. Cao, S. A. G. Lambrechts, M. C. G. Aalders, H. Zhang, *ACS Nano*, 2012, **6**, 4054-4062.
39 C. Wang, L. A. Cheng, Z. A. Liu, *Biomaterials*, 2011, **32**, 1110-1120.
40 J. G. J. Raj, M. Quintanilla, K. A. Mahmoud, A. Ng, F. Vetrone, M. Zourob, *ACS Appl. Mater. Interfaces*, 2015, **7**, 18257-18265.
41 M. Bandini, M. Bianchi, G. Valenti, F. Piccinelli, F. Paolucci, M. Monari, A. U. Ronchi, M. Marcaccio, *Inorg. Chem*., 2010, **49**, 1439-1448.
42 V. Mahalingam, F. Vetrone, R. Naccache, A. Speghini, J. A. Capobianco, *Adv. Mater*., 2009, **21**, 4025-4028.
43 G. Jalani, R. Naccache, D. H. Rosenzweig, S. Lerouge, L. Haglund, F. Vetrone, M. Cerruti, *Nanoscale*, 2015, **7**, 11255-11262.
44 F. Shi, Y. Zhao, *J. Mater. Chem. C*., 2014, **2**, 2198-2203.
45 J. Shen, G. Y. Chen, T. Y. Ohulchanskyy, S. J. Kesseli, S. Buchholz, Z.P. Li, P. N. Prasad, G. Han, *Small*, 2013, **9**, 3213-3217.
46 M. Quintanilla, I. X. Cantarelli, M. Pedroni, A. Speghini, F. Vetrone, *J. Mater. Chem. C*, 2015, **3**, 3108-3113.
47 B. F. Zhang, M. Frigoli, F. Angiuli, F. Vetrone, J. A. Capobianco, *Chemical Communications*, 2012, **48**, 7244-7246.
48 T. Cheng, R. F. Ortiz, K. Vedantham, R. Naccache, F. Vetrone, R.S. Marks, T. W. J. Steele, *Biomacromolecules*, 2015, **16**, 364-373.
49 M. Wozniak, F. Tanfani, E. Bertoli, G. Zolese, J. Antosiewicz, *Biochim. Biophys. Acta, Lipids Lipid Metab.*, 1991, **1082**, 94-100.